International Journal of Technology 15(4) 1133-1147 (2024)
Received November 2022 / Revised January 2023 / Accepted Februari 2023

International Journal of Technology

http://ijtech.eng.ui.ac.id

A Novel Design and Performance Analysis of Piezoelectric Energy Harvester with Application to a Vehicle Suspension System Moving on Uniform Bridges

Muhammad Fathul Hikmawan[1], Budi Azhari[1], Edwar Yazid[1*], Aditya Sukma Nugraha[1], Midriem Mirdanies[1]

[1]*Research Center for Smart Mechatronics,* National Research and Innovation Agency (BRIN), Bandung, 41035, West Java, Indonesia

Abstract. The development of energy recovery systems in vehicles is a form of synergy between energy efficiency and renewable energy to overcome the energy crisis and global warming problems. This paper addresses such challenges by introducing a novel design of a piezoelectric energy harvester (PEH) for a vehicle suspension system. The PEH is designed to capture the linear vibration of the suspension system subjected to road surface roughness and mov**e** on uniform bridges. The vibration is amplified by a pressurized liquid cylinder-piston mechanism which deforms the piezoelectric bar to produce electric power. An additional novel mechanism in the form of a piezoelectric protector is also proposed to avoid physical damage due to excessive unidirectional compressive force as a result of an unpredictable uneven road. Given the key design parameters, the electric power can be harvested up to 67.5 W for a PEH with a span of 150 m of the bridge, a velocity of 40 m/s, and a vehicle mass of 2,691.6 kg.

Keywords: Energy harvesting; Hydraulic mechanism; Piezoelectric; Vehicle suspension

1. Introduction

In vehicle suspension systems, the vibrations produced due to the road surface irregularities, acceleration, and deceleration are considered as energy losses. Researchers have processed and reused it as a new energy source for an energy efficiency and recovery system (e.g., a tuned vehicle damper (Alhumaid, Hess, and Guldiken, 2022; Xie *et al.*, 2020; Pan *et al.*, 2017) and piezoelectric energy harvester (PEH) (Elgamal, Elgamal, and Kouritem, 2024; Akbar *et al.*, 2022; Azangbebil *et al.*, 2019; Taghavifar and Rakheja, 2019; Zhao *et al.,* 2019a; Chen *et al.,* 2016; Hendrowati, Guntur, and Sutantra, 2012; Jeon *et al.,* 2005)). With the piezoelectric transducer, an energy harvester with a specific application to a vehicle suspension system has attracted significant attention (Du *et al.*, 2023; Ghormare, 2022; Sheng *et al.*, 2022; Li *et al.*, 2021; Darabseh *et al.,* 2020; Morangueira and Pereira, 2020; Tavares and Ruderman, 2020; Wang *et al.*, 2020; Lafarge *et al.*, 2019; Shin *et al.*, 2019; Zhao *et al.,* 2019b; Kulkarni *et al.,* 2018; Tao *et al.*, 2017; Wei and Taghavifar, 2017). However, the generated electrical power is still in the mW order. Nowadays, there is an urgent need to enhance the electric power capacity of a PEH. To date, the existing literatures are very limited. A new class of PEH has been proposed, such as: a dual-mass piezoelectric

*Corresponding author's email: edwa005@brin.go.id
doi: 10.14716/ijtech.v15i4.6155

bar harvester with a power up to 738 W (Viet *et al.*, 2017), a two-DoF PEH with the power up to 40 W (Touairi and Mabrouki, 2021), a dual-mass suspension system vibration model with the power up to 102.24 W (Zhao *et al.*, 2019a), and two-way linier beam movements with a power up to 133 μW (Tian *et al.*, 2019). In order to maximize the power generating capacity order to the captured energy, researchers mostly focused on the location of the piezoelectric installation. Due to studies performed by Al-Yafeai, Darabseh, and Mourad (2020) placing a piezoelectric stack in series with a suspension spring system can result in a significant power output when compared to a conventional system (Al-Yafeai, Darabseh, and Mourad, 2020). According to Lafarge *et al.* (2015) installing piezoelectric material between two absorber surfaces produced more energy than placing it on the dampers surface (Lafarge *et al.*, 2015).

This paper enhances the aforementioned research works with the following contributions: (i) a novel design of PEH for a vehicle suspension system is presented, utilizing a pressurized liquid cylinder-piston mechanism to deform the piezoelectric material and generate electricity, (ii) a novel additional mechanism of a piezoelectric protector is proposed to avoid damage due to excessive unidirectional compressive force as a result of an unpredictable uneven road, (iii) the dynamic model of the PEH mounted on a vehicle is improved by transitioning from a mobile quarter-car model to a mobile half-car planar model that considers both the passenger and driver and moves on uniform bridges for more realistic performance (iv) performance of the proposed PEH for energy harvesting using a piezoelectric bar from PZT material is evaluated using intensive numerical simulations, and parametric study [is performed as well to support the results. The paper is organized as follows. Section 2 presents the design concept and system modeling. Section 3 provides results and discussion. Finally, conclusions are in Section 4.

2. Design Concept and System Modelling

The PEH is proposed to be universally used on a wide range of vehicle suspension types. However, the space available on the suspension section is limited. Also, the vibration level experienced by the suspension is different for every vehicle. It leads to variations of load exerted on the piezoelectric transducer. To harvest the vibration energy optimally, an effective mechanism of the PEH is designed to address those challenges.

2.1. Design Concept

Figure 1a shows the proposed PEH design concept (Figure 1b) mounted on a vehicle suspension system. There are two main developed mechanisms: force magnification and piezoelectric protector mechanism (Figure 1c). The former is designed to amplify the excitation force through a linear-spring mounted on the suspension system. It works based on a pressurized liquid cylinder-piston mechanism known as a hydraulic system, consisting of the master cylinder and caliper cylinder components. Due to the vehicle suspension's limited space, the PEH that can be mounted onto the suspension system is limited in volume. Thus, the master cylinder components with small volumes and easily attached must be chosen.

However, some factors such as road surface roughness, traffic conditions, and vehicle speed dynamics may significantly affect excitation force. If the road surface is flat with congested traffic conditions, the vehicle suspension's excitation force may be weak. Thus, the force magnification mechanism must be set to effectively capture the suspension's vibration while amplifying its magnitude simultaneously. Meanwhile, the piezoelectric protector is an additional mechanism to avoid piezoelectric damage due to excessive

unidirectional compressive force as a result of an unpredictable uneven road. It uses springs as the main component for regulating the pressure that deforms the piezoelectric.

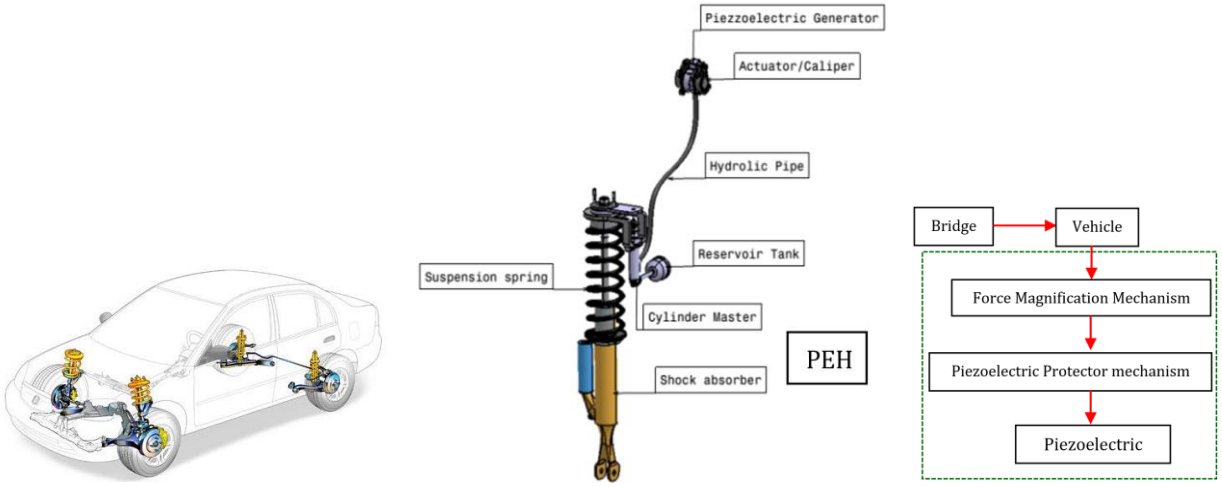

(a) (b) (c)

Figure 1 System: (a) suspension [Adapted from www.pakwheels.com (Ali, 2015)], (b) PEH, (c) diagram block of modeling

2.2. System Modelling

The model of the overall system in Figure 1a comprises three main subsystems: the dynamics of the bridge, the vehicle, and the PEH. In this subsection, each will be detailed, and the parameter values of the respective subsystems will be tabulated afterward.

2.2.1. Modelling of Force Magnification Mechanism

Figure 2 shows the overall structure and working principle of the proposed force magnification mechanism, which is the main subsystem of the PEH. The spring force *F* generated by the vehicle suspension's vibration is transmitted to the large piston, which moves the master cylinder and produces force *F1*. The force is then transferred to the fluid in the closed channel. The fluid will move the small piston and produce *F2* in the caliper. The force *F2* will deform the piezoelectric bar and generate electrical energy. In short, this mechanism applies Pascal's Law (Equations 1-2). By taking into account the cross-sectional area of both pistons, *A1* and *A2*, the value of *F2* can then be calculated,

$$F2 = F1 \cdot \left(\frac{A2}{A1} \right) \tag{1}$$

The ratio of cross-sectional area is denoted by $n_p = A2/A1$ where $n_p > 1$ so the excitation force in the master cylinder into the caliper can be magnified. This magnified force will deform the piezoelectric at the end of the piston in the caliper. By taking the effect of friction force between piston and cylinder and working fluid mass in the pressurized cylinder-piston system are not accounted for, the ratio of the big piston of master cylinder *S1* and small piston of caliper *S2* to the respective cross-sectional area *A1* and *A2* is,

$$\frac{S1}{S2} = \frac{A2}{A1} = \frac{F2}{F1} \tag{2}$$

Since the excitation force exerted by the vehicle suspension system on the PEH is random, impulsive impact force can occur anytime. It then becomes an important consideration for PEH design. A novel design of a piezoelectric protector mechanism is proposed to minimize physical damage. Figure 2 provides the design concept and its

components. If the magnitude of force F approaches or exceeds the limit of compressive strength of piezoelectric material, the linear spring will be compressed accordingly. The push rod then sticks to the stopper and discharges to press the piezoelectric. Thus, the piezoelectric will always be within its strength limit and a safe mode.

2.2.2. Modelling of PEH

Since the PEH is mounted onto the existing vehicle's suspension, it can be considered as two main structures: super- and sub-structure. The former is a vehicle, while the latter is a hydraulic system-based PEH. The piezoelectricity cylinder-piston mechanism depicted in Figure 3a can be simplified as a translational lumped mass and is shown in Figure 3b. It consists of an equivalent mass m_{eq}, damping coefficient $c_{eq,}$ and spring constant k_{eq}. Two external springs are from master cylinder k_t and piezoelectric protector k_s. If the piston thickness and its mass density, $t_{cp,}$ and ρ_{cp} are respectively defined, then the mass of the small piston under pressurized working fluid can be computed using Equation 3,

$$m_{eq} = \rho_{cp} \cdot V_{cp1} = \rho_{cp} \cdot \left(\pi^{d_{cp1}^2} / 4 \cdot t_{cp1} \right) \tag{3}$$

A big piston deforms the piezoelectric transducer in Figure 2c through piston extension where its spring constant is not considered. Spring stiffness k_{pb} of the big piston may be computed using Equation 4,

$$k_{pb} = \frac{E_{pb} w_{pb} t_{pb}}{l_{pb}} \tag{4}$$

Considering the working fluid, the small piston can be modeled as a spring on a mass. The equivalent spring stiffness k_{eq} can be calculated using Equation 5.

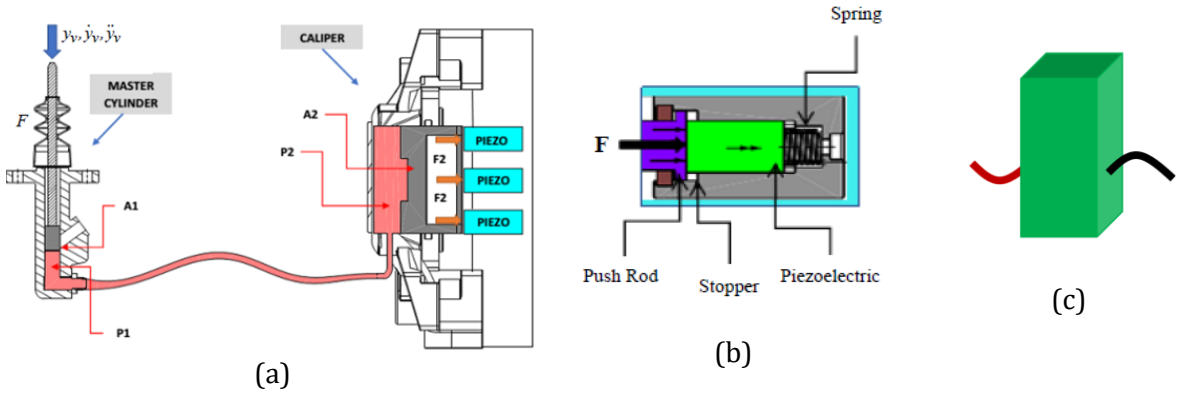

Figure 2 Overall structure and working principle (a) proposed force magnification mechanism (b) Proposed piezoelectric protector mechanism (c) Piezoelectric bar

$$k_{eq} = \frac{E_p w_{pb} t_{pb}}{\left(n_p^{\,4} l_{pb} \right)} \tag{5}$$

When the work done by the spring force is converted into electricity, there is an equivalent electric resistance. The electrical damping coefficient c_{eq} can be derived as follows (Aouali *et al.,* 2021; Pasharavesh, Moheimani, and Dalir, 2020; Wu, Wang, and Xie, 2015; Xie and Wang, 2015),

$$C_{eq} = \frac{n_p^{\,2} d_{33}^{\,2} k_{eq}^{\,2}}{\left(\pi^2 c_a f \right)} \tag{6}$$

Equation 6 contains three important variables: d_{33} is the piezoelectric strain constant in the polling direction, c_a is the electrical capacity of the piezoelectric bar, and f is the natural vibration frequency of the system.

Once the equivalent mass m_{eq}, spring constant k_{eq}, and damping coefficient c_{eq} are obtained, the proposed PEH results in a damped single-degree-of-freedom system subjected to the road surface roughness. Considering the equivalent magnified force $F_m(t)$ at the PEH as expressed in Equation 7, the electrical charge that can be stored by the piezoelectric bar is calculated using Equation 8,

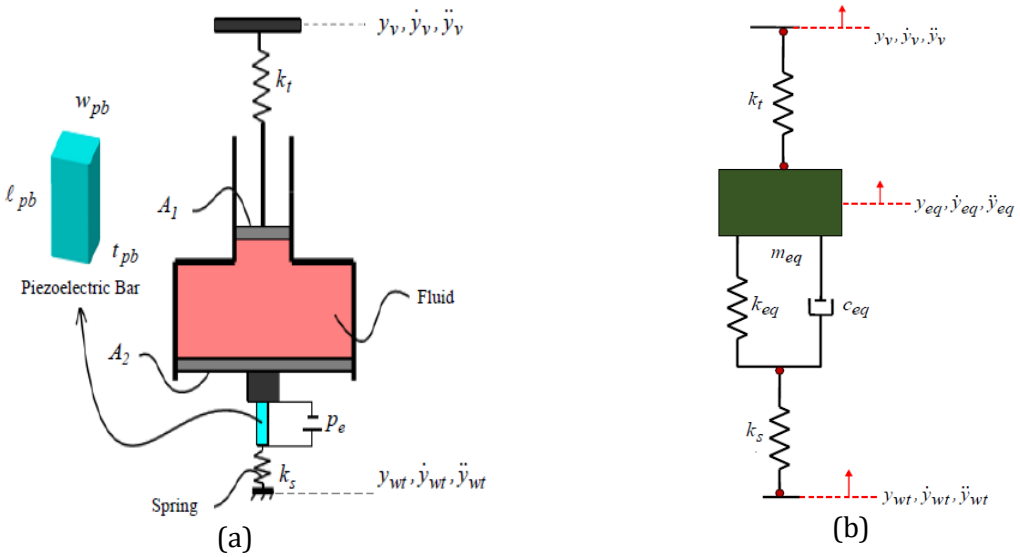

Figure 3 PEH model (a) Cylinder-piston mechanism (b) Equivalent model of the proposed PEH

$$F_m(t) = n_p \left\{ k_{eq} y_{eq}(t) - c_{eq} \dot{y}_{eq}(t) \right\}, \tag{7}$$

$$Q_{ep}(t) = d_{33} F_m(t). \tag{8}$$

Equation 7 and Figure 3b contain some important parameters: y_v and y_{wt} are displacements of the vehicle body and wheel tire, respectively, in the area where the PEH is mounted, y_{eq} is the displacement of the PEH, and n is the magnification factor (cross-sectional area ratio). The electrical current resulted by the piezoelectric bar can be calculated by deriving the electrical charge in Equation 8 with respect to time,

$$I_{ep}(t) = d_{33} n_p \left\{ k_{eq} \dot{y}_{eq}(t) - c_{eq} \ddot{y}_{eq}(t) \right\} \tag{9}$$

The electrical voltage resulted by the piezoelectric bar can be found by dividing the electrical charge Q_{ep} in Equation 8 over electrical capacity of the piezoelectric material c_a,

$$V_{ep}(t) = \frac{d_{33} f_m(t)}{c_a} \tag{10}$$

Generated electrical power is then obtained by multiplying the electrical current in Equation 9 and electrical voltage in Equation 10 with the number of piezoelectric p,

$$P_{ep}(t) = p I_{ep}(t) V_{ep}(t) \tag{11}$$

Equations 8-11 reflect that the outputs of PEH are electrical parameters such as electrical charge, current, voltage, and power. In particular, electrical charge Q_{ep} is seen as a very instrumental parameter and must be produced optimally. The RMS of the electric power within a predefined time duration can be then determined by using Equation 12,

$$P_{rms} = \sqrt{\frac{1}{\tau}\int_0^{\tau} P_{ep}{}^2(t)\,dt} \tag{12}$$

2.2.3. Modelling of Bridge Dynamics Traversed by a Mobile Half-Car Planar Model

Quarter-car model is the common model employed. However, such a model type is considered inadequate for many realistic cases, particularly for analyzing the total vehicle dynamics. In this paper, the vehicle consisting of the driver and passenger is modeled as a mobile half-car planar model, as depicted in Figure 4a. The vehicle moves on a bridge above the uneven road surface. The case becomes transverse elastic deformation of the bridge traversed by a mobile half-car planar model carrying the PEHs. They are modeled in Figure 4b. In deriving the governing equations of motion, simplifications and assumptions are defined:

1. The overall system is modeled in linear behavior.
2. A mobile half-car planar model has six DoFs, which consist of a body, two PEHs, two-wheel tires, a driver, and a passenger. The vehicle body is constrained to have the vertical motion (bounce) and the angular motion (pitch), where every wheel-tire bounces in its respective coordinate. Also, the driver and the passenger are considered to have only their vertical oscillations.
3. The PEH is mounted between the vehicle body and the wheel-tire in front or rear positions.
4. Passenger seats, suspension, and wheel-tire systems are modeled as a combination of linear springs and viscous dampers which are connected in parallel arrangements.
5. The resilience and damping of the suspension and wheel-tire systems are expected to be sufficient so as to be more realistic models for simulation and analysis.
6. The wheel-tire system is assumed to be in contact with the surface of the uneven road at all times.

To derive the motion equations of the overall system, the energy method is employed. By defining *x* as the axis along the length of the beam measured from the left to right end support, and *t* as the travel time, then *y(x,t)* can be characterized as the vertical deformation of the bridge all the way of the undeformed neural axis of the bridge as depicted by Figure 4b. The kinetic and potential energies of the overall system in Figure 4a using linear strains assumption are given by Equations 13-14, respectively. Both equations belong to the bridge, vehicle body (bounce and pitch), PEH, wheel-tire (front and rear), driver, and passenger. Parameter ρ in Equation 13 is the mass density per unit length of the uniform beam, *EI* in Equation 14 denotes the flexural rigidity of the beam, while *H(x)* represents the Heaviside function. In particular, Equation 14 contains variables $\xi f(t)$ and $\xi r(t)$, which point out the locations of the contact points of the front and rear tires with the bridge surface.

$$T_{os} = \frac{1}{2}\left(\int_0^L \rho\left(\dot{y}_b{}^2(x,t)\,dx + m_{wt_f}\dot{y}_{wt_f}{}^2(t) + m_{wt_r}\dot{y}_{wt_r}{}^2(t)\right) + m_{eq_f}\dot{y}_{eq_f}{}^2(t) + m_{eq_r}\dot{y}_{eq_r}{}^2(t) + m_v\dot{y}_v{}^2(t) + J_v\dot{\theta}_v{}^2(t) + m_d\dot{y}_d{}^2(t) + m_p\dot{y}_p{}^2(t)\right), \tag{13}$$

$$U_{os} = \frac{1}{2}\begin{pmatrix} \int_0^L EI\left(y_b{}''^2(x,t)\right)dx + k_{wt_f}\left(y_{wt_f}(t) - y_b\left(\xi_f(t),t\right) - \mathrm{r}\right)^2 H\left(x-\xi_f(t)\right) + k_{wt_r}\left(y_{wt_r}(t) - y_b\left(\xi_r(t),t\right) - \mathrm{r}\right)^2 H\left(x-\xi_r(t)\right) \\ + k_{tot_{2f}}\left(y_{eq_f}(t) - \mathrm{y}_{\mathrm{wt_f}}(t)\right)^2 + k_{tot_{2r}}\left(y_{eq_r}(t) - \mathrm{y}_{\mathrm{wt_r}}(t)\right)^2 + k_{tot_{1f}}\left(y_v(t) - \mathrm{y}_{\mathrm{eq_f}}(t) + b_1\theta_v(t)\right)^2 \\ + k_{tot_{1r}}\left(y_v(t) - \mathrm{y}_{\mathrm{eq_r}}(t) - b_2\theta_v(t)\right)^2 + k_d\left(\mathrm{y_d}(t) - y_v(t) + d_1\theta_v(t)\right)^2 + k_p\left(\mathrm{y_p}(t) - y_v(t) - d_2\theta_v(t)\right)^2 \end{pmatrix}, \tag{14}$$

$$\xi_f(t) = u(t) + b_1, \quad \xi_r(t) = u(t) - b_2. \tag{15}$$

Rayleigh's dissipation function and generalized force are expressed in Equations 16-18,

$$R_{OS}=\frac{1}{2}\begin{Bmatrix} c_b\dot{y}_b{}^2+c_{wt_f}\left(\dot{y}_{wt_f}(t)\text{-}\dot{y}_b\left(\xi_f(t),t\right)\text{-}\dot{r}\right)^2H\left(x\text{-}\xi_f(t)\right)+c_{wt_r}\left(\dot{y}_{wt_r}(t)\text{-}y_b\left(\xi_r(t),t\right)\text{-}\dot{r}\right)^2H\left(x\text{-}\xi_r(t)\right) \\ +c_{eq_f}\left(\dot{y}_{eq_f}(t)\text{-}\dot{y}_{wt_f}(t)\right)^2+c_{eq_r}\left(\dot{y}_{eq_r}(t)\text{-}\dot{y}_{wt_r}(t)\right)^2+c_{sb_f}\left(\dot{y}_v(t)\text{-}\dot{y}_{eq_f}(t)+b_1\dot{\theta}_v(t)\right)^2 \\ c_{sb_r}\left(\dot{y}_v(t)\text{-}\dot{y}_{eq_r}(t)\text{-}b_2\dot{\theta}_v(t)\right)^2+c_d\left(\dot{y}_d(t)\text{-}\dot{y}_v(t)+d_1\dot{\theta}_v(t)\right)^2+c_p\left(\dot{y}_p(t)\text{-}\dot{y}_v(t)\text{-}d_2\dot{\theta}_v(t)\right)^2 \end{Bmatrix}, \tag{16}$$

$$Q_i=\int_0^L\varphi_i(x)\,f_g(x,t)\,dx,\quad i=1,2,\cdots,n, \tag{17}$$

$$\begin{aligned} f_g(x,t)&=-\left(m_{wt_f}+m_v\frac{b_2}{b_1+b_2}+m_d\frac{b_2+d_1}{b_1+b_2}\text{-}m_p\frac{b_2\text{-}d_2}{b_1+b_2}\right)g\,H\left(x\text{-}\xi_f(t)\right)\text{-}\left(m_{wt_r}+m_v\frac{b_1}{b_1+b_2}+m_d\frac{b_1\text{-}d_1}{b_1+b_2}+m_p\frac{b_1+d_2}{b_1+b_2}\right)g\,H\left(x\text{-}\xi_r(t)\right) \\ &=-\left(f_{g_f}H\left(x\text{-}\xi_f(t)\right)+f_{g_r}H\left(x\text{-}\xi_r(t)\right)\right). \end{aligned} \tag{18}$$

By considering the Galerkin approximation, $y(x,t)$ is written in Equation 19, where $\phi_i(x)$ presents mode shapes and $q_i(t)$ points out the generalized coordinates for the elastic deflection of the beam element. Orthogonality conditions are given by Equation 20, where the term δ_{ij} denotes the Kronecker delta for $i,j=1,2,..,n$,

$$y(x,t)=\sum_{i=1}^{n}\phi_i(x)q_i(t), \tag{19}$$

$$\int_0^L\rho\phi_i(x)\phi_j(x)dx=N_i\,\delta_{ij},\int_0^L EI\phi_i{}''(x)\phi_j{}''(x)dx=S_i\,\delta_{ij} \tag{20}$$

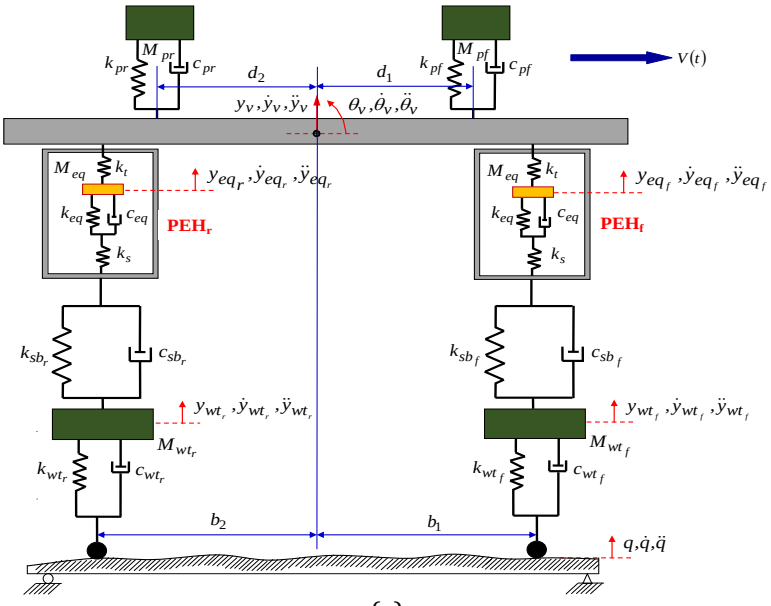

Figure 4 Vehicle system model (a) the bridge traversed by a mobile half-car planar model (b) transverse elastic deformation of the bridge traversed by a mobile half-car planar model

Defining the eight state variables as in Equation 21, Lagrange's equations for those variables can be expressed in Equations 22-23,

$$p(t)=\left\{y_{wt_f}(t)\quad y_{wt_r}(t)\quad y_{eq_f}(t)\quad y_{eq_r}(t)\quad y_b(t)\quad \theta_b(t)\quad y_d(t)\quad y_p(t)\right\}^T. \tag{21}$$

$$\frac{d}{dt}\left(\frac{\partial T_{OS}}{\partial P_k(t)}\right)-\frac{\partial T_{OS}}{\partial P_k(t)}+\frac{\partial U_{OS}}{\partial P_i(t)}+\frac{\partial R_{OS}}{\partial P_k(t)}=0,\quad k=1,2,\cdots,6\quad, \tag{22}$$

$$\frac{d}{dt}\left(\frac{\partial T_{OS}}{\partial q_k(t)}\right)-\frac{\partial T_{OS}}{\partial q_k(t)}+\frac{\partial U_{OS}}{\partial q_i(t)}+\frac{\partial R_{OS}}{\partial q_k(t)}=Q_i,\quad i=1,2,\cdots,n. \tag{23}$$

Finally, motion equations of the overall system can be derived in general forms,

1. The vertical motion (bounce) for the driver is given by,

$$m_d\ddot{y}_d+c_d\left(\dot{y}_d-\dot{y}_v+d_1\dot{\theta}_v\right)+k_d\left(y_d-y_v+d_1\theta_v\right)=0. \tag{24}$$

2. The vertical motion (bounce) for the passenger is presented by,

$$m_p\ddot{y}_p+c_p\left(\dot{y}_p-\dot{y}_v+d_2\dot{\theta}_v\right)+k_p\left(y_p-y_v+d_2\theta_v\right)=0\ . \tag{25}$$

3. The vertical motion (bounce) for the vehicle is defined as,

$$\begin{aligned}&m_v\ddot{y}_v+c_d\left(\dot{y}_d-\dot{y}_v+d_1\dot{\theta}_v\right)+c_p\left(\dot{y}_p-\dot{y}_v-d_2\dot{\theta}_v\right)+c_{sb_f}\left(\dot{y}_v-\dot{y}_{eq_f}+b_1\dot{\theta}_v\right)+c_{sb_r}\left(\dot{y}_v-\dot{y}_{eq_r}-b_2\dot{\theta}_v\right)\\&+k_d\left(y_d-y_v+d_1\theta_v\right)+k_p\left(y_p-y_v-d_2\theta_v\right)+k_{sb_f}\left(y_v-y_{eq_f}+b_1\theta_v\right)+k_{sb_r}\left(y_v-y_{eq_r}-b_2\theta_v\right)=0.\end{aligned} \tag{26}$$

4. The vertical motion for the front PEH is,

$$m_{eq_f}\ddot{y}_{eq_f}+c_{sb_f}\left(\dot{y}_v-\dot{y}_{wt_f}+b_1\dot{\theta}_v\right)+c_{eq_f}\left(\dot{y}_{eq_f}-\dot{y}_{wt_f}\right)+k_{tot_{1f}}\left(y_v-y_{wt_f}+b_1\theta_v\right)+k_{eq_f}\left(y_{eq_f}-y_{wt_f}\right)=0. \tag{27}$$

5. The angular motion (pitch) for the vehicle can be expressed as,

$$\begin{aligned}&J_v\ddot{\theta}_v+c_dd_1\left(\dot{y}_d-\dot{y}_v+d_1\dot{\theta}_v\right)-c_pd_2\left(\dot{y}_p-\dot{y}_v-d_2\dot{\theta}_v\right)+c_{sb_f}b_1\left(\dot{y}_v-\dot{y}_{eq_f}+b_1\dot{\theta}_v\right)-c_{sb_r}b_2\left(\dot{y}_v-\dot{y}_{eq_r}-b_2\dot{\theta}_v\right)\\&+k_dd_1\left(y_d-y_v+d_1\theta_v\right)-k_pd_2\left(y_p-y_v-d_2\theta_v\right)+k_{sb_f}b_1\left(y_v-y_{eq_f}+b_1\theta_v\right)-k_{sb_r}b_2\left(y_v-y_{eq_r}-b_2\theta_v\right)=0.\end{aligned} \tag{28}$$

6. The vertical motion for the rear PEH is,

$$m_{eq_r}\ddot{y}_{eq_r}+c_{sb_r}\left(\dot{y}_v-\dot{y}_{wt_r}-b_2\dot{\theta}_v\right)+c_{eq_r}\left(\dot{y}_{eq_r}-\dot{y}_{wt_r}\right)+k_{tot_{1r}}\left(y_v-y_{wt_r}-b_2\theta_v\right)+k_{eq_r}\left(y_{eq_r}-y_{wt_r}\right)=0. \tag{29}$$

7. The vertical motion for the front wheel-tire can be written as,

$$m_{wt_f}\ddot{y}_{wt_f}+c_{eq_f}\left(\dot{y}_{eq_f}-\dot{y}_{wt_f}\right)+c_{wt_f}\left(\dot{y}_{wt_f}-\dot{r}\right)+k_{tot_{2f}}\left(y_{eq_f}-y_{wt_f}\right)+k_{eq_f}\left(y_{wt_f}-r\right)=0. \tag{30}$$

8. The vertical motion for the rear wheel-tire can be written as,

$$m_{wt_r}\ddot{y}_{wt_r}+c_{eq_r}\left(\dot{y}_{eq_r}-\dot{y}_{wt_r}\right)+c_{wt_r}\left(\dot{y}_{wt_r}-\dot{r}\right)+k_{tot_{2r}}\left(y_{eq_r}-y_{wt_r}\right)+k_{eq_r}\left(y_{wt_r}-r\right)=0. \tag{31}$$

9. The equation motion of the bridge is,

$$N_i\ddot{q}_i(t)+S_iq_i(t)+D_1\varphi_i\left(\xi_f(t)\right)\begin{Bmatrix}f_{g_1}+c_{wt_f}\left(\dot{y}_v\left(\xi_f(t),t\right)D_1\text{-}\dot{y}_{wt_f}\right)\\+k_{wt_f}\left(y_v\left(\xi_f(t),t\right)D_1\text{-}y_{wt_f}\right)\end{Bmatrix}+D_2\varphi_i\left(\xi_r(t)\right)\begin{Bmatrix}f_{g_2}+c_{wt_r}\left(\dot{y}_v\left(\xi_r(t),t\right)D_2\text{-}\dot{y}_{wt_r}\right)\\+k_{wt_r}\left(y_v\left(\xi_r(t),t\right)D_2\text{-}y_{wt_r}\right)\end{Bmatrix},i=1,2,\cdots,n. \tag{32}$$

Parameter k_{tot1} is equivalent spring stiffness between shock-breaker with external spring of master cylinder k_t, k_{tot2} is equivalent spring stiffness between wheel-tires with external spring of piezoelectric protector k_s while two coefficients D_1 and D_2 denote the predefined interval of the motion of the vehicle. The roughness of road surface (Wei and Taghavifar, 2017),

$$\dot{r}+2\dot{r}+2\pi f_0r=2\pi n_0\sqrt{g_q(n_0)v(t)w(t)}. \tag{33}$$

$G_q(n_0)$ indicates the roughness coefficient of the road surface, n_0 refers to a reference spatial frequency with a value of 0.1 m^{-1}, f_0 is a minimal boundary frequency with a value of 0.0628 Hz, $v(t)$ denotes the vehicle velocity, and $w(t)$ presents a zero-mean white noise.

2.2.4. Numerical Solver

Equations 24-32 form a system of nine second-order coupled differential equations. They could be written in the state-space model by converting all equations into first-order differential equation systems. Consequently, state variables become (2+(2·DOF)+n) as the following,

$$\left\{ x_1 = r \quad x_3 = y_{wt_f} \quad x_5 = y_{wt_r} \quad x_7 = y_{eq_f} \quad x_9 = y_{eq_r} \quad x_{11} = y_v \quad x_{13} = \theta_v \quad x_{15} = y_d \quad x_{17} = y_p \quad x_{19} = q_n \right\}, \tag{34}$$

$$\Downarrow$$

$$\left\{ \dot{x}_2 = \dot{r} \quad \dot{x}_4 = \ddot{y}_{wt_f} \quad \dot{x}_6 = \ddot{y}_{wt_r} \quad \dot{x}_8 = \ddot{y}_{eq_f} \quad \dot{x}_{10} = \ddot{y}_{eq_r} \quad \dot{x}_{12} = \ddot{y}_v \quad \dot{x}_{14} = \ddot{\theta}_v \quad \dot{x}_{16} = \ddot{y}_d \quad \dot{x}_{18} = \ddot{y}_p \quad \dot{x}_{20} = \ddot{q}_n \right\}.$$

$$\left\{ \begin{array}{llll} \dot{x}_2 = F_1(t, x_1) & \dot{x}_{12} = F_6(x_7, x_8, x_{10}, x_{11}, x_{12}, x_{13}, x_{14}, x_{16}, x_{17}, x_{18}) & x_2 = F_{11}(x_1) & x_{12} = F_{16}(x_{11}) \\ \dot{x}_4 = F_2(x_3, x_4, x_7, x_8, x_9, x_{10}) & \dot{x}_{14} = F_7(x_7, x_8, x_9, x_{10}, x_{11}, x_{12}, x_{13}, x_{14}, x_{15}, x_{16}, x_{17}, x_{18}) & x_4 = F_{12}(x_3) & x_{14} = F_{17}(x_{13}) \\ \dot{x}_6 = F_3(x_1, x_2, x_5, x_6, x_7, x_8, x_9, x_{10}) & \dot{x}_{16} = F_8(x_{11}, x_{12}, x_{13}, x_{14}, x_{15}, x_{16}) & x_6 = F_{13}(x_5) & x_{16} = F_{18}(x_{15}) \\ \dot{x}_8 = F_4(x_3, x_4, x_7, x_8, x_{11}, x_{13}, x_{14}) & \dot{x}_{18} = F_9(x_{11}, x_{12}, x_{13}, x_{14}, x_{17}, x_{18}) & x_8 = F_{14}(x_7) & x_{18} = F_{19}(x_{17}) \\ \dot{x}_{10} = F_5(x_5, x_6, x_9, x_{10}, x_{11}, x_{12}, x_{13}, x_{14}) & \dot{x}_{20} = F_{10}(x_3, x_4, x_5, x_6, x_{11}, x_{12}) & x_{10} = F_{15}(x_9) & x_{20} = F_{20}(x_{19}) \end{array} \right\}, \tag{35}$$

$$\begin{aligned} & t_{i+1} = t_i + \Delta_t, \\ & \dot{x}_2(t_{i+1}) = \dot{x}_2(t_i) + F_1\left(x_1(t_i)\right) \cdot \Delta_t, \\ & \dot{x}_4(t_{i+1}) = \dot{x}_4(t_i) + F_2\left(x_3(t_i), x_4(t_i), x_7(t_i), x_8(t_i), x_9(t_i), x_{10}(t_i)\right) \cdot \Delta_t, \\ & \vdots \\ & \dot{x}_{20}(t_{i+1}) = \dot{x}_{20}(t_i) + F_{10}\left(x_3(t_i), x_4(t_i), x_5(t_i), x_6(t_i), x_{11}(t_i), x_{12}(t_i)\right) \cdot \Delta_t, \\ & x_2(t_{i+1}) = x_1(t_i) + F_1\left(x_1(t_{i+1})\right) \cdot \Delta_t, \\ & x_4(t_{i+1}) = x_3(t_i) + F_{12}\left(x_3(t_{i+1})\right) \cdot \Delta_t, \\ & \vdots \\ & x_{20}(t_{i+1}) = x_{19}(t_i) + F_{20}\left(x_{19}(t_{i+1})\right) \cdot \Delta_t. \end{aligned} \tag{36}$$

From Equation 34, the system of first-order differential equations can be arranged in Equation 35. Considering the computational time and accuracy, the time step Δt is selected as 0.001 s. Consequently, the displacements and velocities of the system at the time t_{i+1} can be arranged as in Equation 36. By assuming that the system is in an equilibrium position at $i=0$ and $t_0=0$ *s*, the initial conditions of all are equal to zero.

3. Results and Discussion

The proposed PEH's performance is evaluated using important design factors: the ratio of piston cross-sectional area, vehicle velocity, and road roughness coefficient. Dynamic responses of displacement, velocity, and acceleration in all nodal coordinates of the half-car planar model, particularly at the point of the PEH mounted on the vehicle suspension, are used. For vehicle dynamics, the road roughness coefficient refers to ISO/TC108/SC2N67 (Wei and Taghavifar, 2017), in which only the classes B, E, and H are used, with roughness coefficient ($G_q(n_0)$, in cm^3) are 64; 4,096; and 65,536 respectively. Meanwhile, Tables 1 and 2 list the beam and vehicle parameters. Dimension and material properties of the PEH are listed in Table 3. The harvested electric power is expressed in RMS value.

3.1. Dynamic Responses Analysis

Results are obtained by setting the numerical variables in simulations such as: (1) a random Gaussian white noise with a zero mean shown in Figure 5a, (2) road surface roughness of the car on the road in the class of B for 10 seconds are depicted in Figure 5b, (3) Two types of velocity are used in terms of variable and constant velocities as, where the former is shown in Figure 6a, and the latter is set to be constant of 30 m/s, (4) parameters of the bridge, vehicle, and PEH are based on Tables 1-3. Dynamic displacements are displayed in Figures 6b. Each figure compares the displacement of respective subsystems under both velocities. However, it should be noted that the values are selected only to show

the dynamic characteristics. Any arbitrary values can be chosen as long as the time trajectory of the vehicle moving on the bridge is sufficient. Figure 7 reveals that the developed motion equations with the numerical solver can capture the dynamics of the overall system. The dynamic displacement obtained from variable and constant velocities is different. An amplification factor is produced when the maximum value of each displacement is compared. The ratio is averagely found around 1.23. It can be a variation if the trajectory profile is varied accordingly. However, those figures are intended to demonstrate the effect of velocity on the generated electrical power of the proposed PEH model, as justified by Figure 8a.

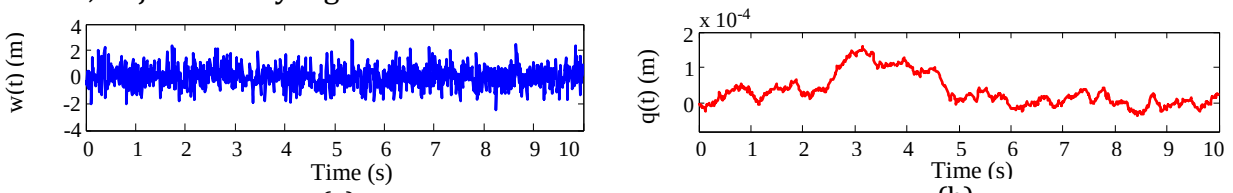

Figure 5 Road data (a) Gaussian white noise with zero mean value (b) road surface roughness

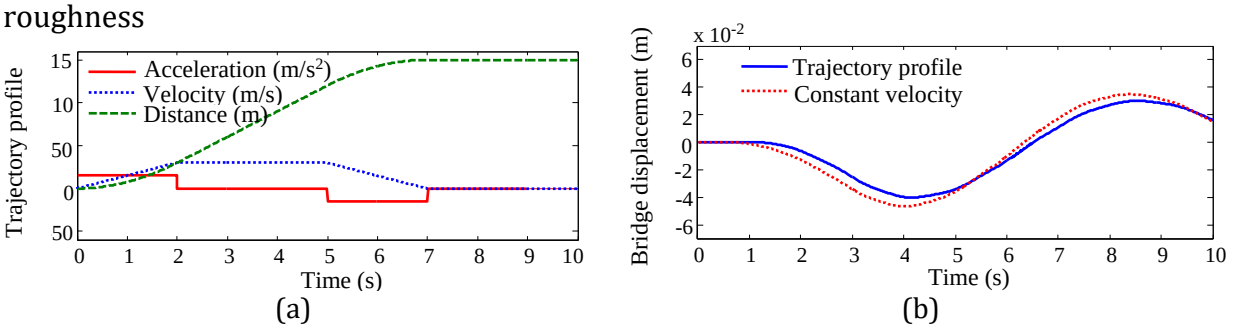

Figure 6 Vehicle and bridge system (a) Trajectory profile for vehicle (b) Bridge displacements

3.2. Parametric Study for PEH

Three key design parameters are chosen: vehicle speed variations, road roughness coefficient, and ratio of the cross-sectional area of the piston. Each variation is tested with three white noise time series to check the robustness of the generated electric power. The white noise has a similar mean value with different intensities, shown in Figure 8b respectively. The first parametric study involves variations in vehicle velocity and its effect on the harvested electric power, while keeping the road roughness coefficient in the C class and maintaining a piston cross-sectional area ratio of 4. The piezoelectric bar and the cylinder-piston dimensions are based on Tables 2-3. The results show that the highest RMS of the generated power is 135 W. From Figure 9a, it can be seen that the increase in vehicle velocity is followed by the increase of P_{rms}. The increment has a linear form. This finding owes to the fact that an increase in velocity leads to an increase in dynamic displacements of the bridge and suspension system, respectively. As a result, the dynamic displacement of the equivalent model of the cylinder-piston mechanism and piezoelectric bar (PEH) in Figure 3, either in the front or rear parts increases correspondingly. Those increments correspond to the increase in charge, voltage, current, and generated electric power of the PEH as indicated by Equations 9-12. Under three white noise time series, the difference slightly deviates within 6% for the generated electrical power. Thus, the proposed PEH model is less sensitive to noise variances.

In the next case, we examine variations in the road roughness coefficient while keeping the vehicle velocity at 40 m/s and the cross-sectional area ratio at 4. Road-roughness

coefficients are based on ISO/TC108/SC2N67 (Class A-H). Piezoelectric bar dimensions and piston-cylinder dimensions are still based on Table 3. The results are displayed in Figure 9b. Similar to the previous variation, an increase in the road roughness coefficient results in an increase in the RMS of the electric power generated by the proposed PEH. However, this increment follows a nonlinear form. The results show that the highest RMS of the generated power is 230 W. However, this value is only found on a very rough road. Such a road may be found as off-road, which is not common as a public road. City road is commonly found in the range of class A to class D so the road-roughness coefficients are considered in those ranges. In this variation, the proposed PEH model is also less sensitive to noise variations. The difference is within 7.5%.

Table 1 Beam parameters

Parameter	Value
Beam length (m)	150
Mass density (kg/m^3)	20,000
Modulus of elasticity of the beam (N/m^2)	2.07e^{11}
Moment of inertia (m^4)	0.261
Damping Coefficient (N.s/m)	2,625

Table 2 Vehicle parameters

Parameter	Value			
	Inertia (kgm^2)	Mass (kg)	Damping (Ns/m)	Stiffness (N/m)
Driver		m_d =112.5	c_d =75.3	k_d =21,000
Passenger		m_p =112.5	c_p =93.15	k_p =21,000
Body	J_s =5,149.575	m_s =112.5		
Front Axle			c_{sbf} =1,785	k_{sbf} =10,023.3
Rear Axle			k_{sbr} =1,500	k_{sbr} =27,922.5
Front Tire		m_{wtf} =130.725	c_{wtf} =21.9	k_{wtf} =151,672.5
Rear Tire		m_{wtr} =210.6	c_{wtr} =21.9	k_{wtr} =151,672

Table 3 Property and dimension of a piezoelectric bar (Piezo, n.d.)

Item	Symbol	Value
Piezoelectric number	p	8
Piezoelectric dimension (m)	a x b x h	0.01 x 0.01 x 0.18
Piezoelectric density (kg/m^3)	P	7,900
Modulus Young (N/m^2)	Ep	4.4e^{10}
Piezoelectric strain constant in the polling direction (N/C)	d_{33}	3e^{-10}
Electrical capacity for the piezoelectric (F)	C_v	6.5e^{-6}

The last case is variations of piston cross-sectional area ratio to the harvested electric power by keeping the vehicle velocity of 30 m/s, and road roughness coefficients in the class of C. The results are displayed in Figure 9c. A nonlinear relation between the RMS of the electric power generated by the proposed PEH and the piston cross-sectional area ratio is found. The results show that the highest RMS of the generated power is 93.5 W under piezoelectric bar and cylinder-piston dimensions in Table 2. This is to be expected since the increase of cross-sectional area ratio n_p decreases the deflection of the PEH. This can be referred to as magnified force $F_m(t)$ in Equation 7.

Since the force increases with the ratio of n, then the P_{rms} increases up to a certain limit. When the ratio of n_p is at higher values, the equivalent damping coefficient c_{eq} becomes predominantly, and the P_{rms} decrease according to Equation 6. Hence, the optimum value of n_p is selected to be 4, which can still be accommodated in the design. For this variation, the proposed PEH model also seems less sensitive to the noise variations as in the previous case. The difference is found within 8.7% for the generated electrical power. This result

suggests that the proposed PEH is robust due to the deviation being relatively low to the variations of white noise as an environmental factor.

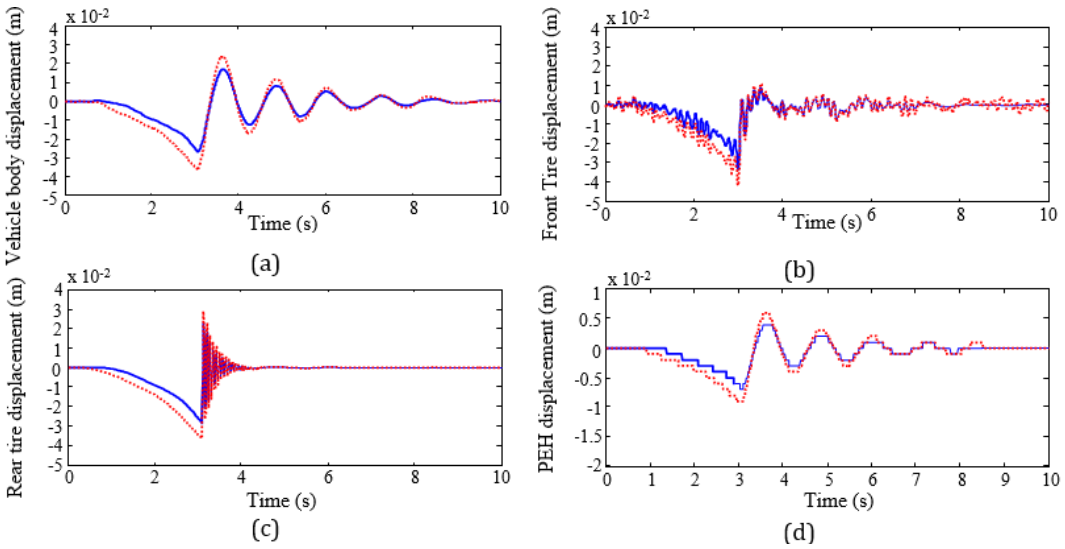

Figure 7 Dynamic displacements of (a) vehicle body (b) front tire (c) rear tire (d) PEH

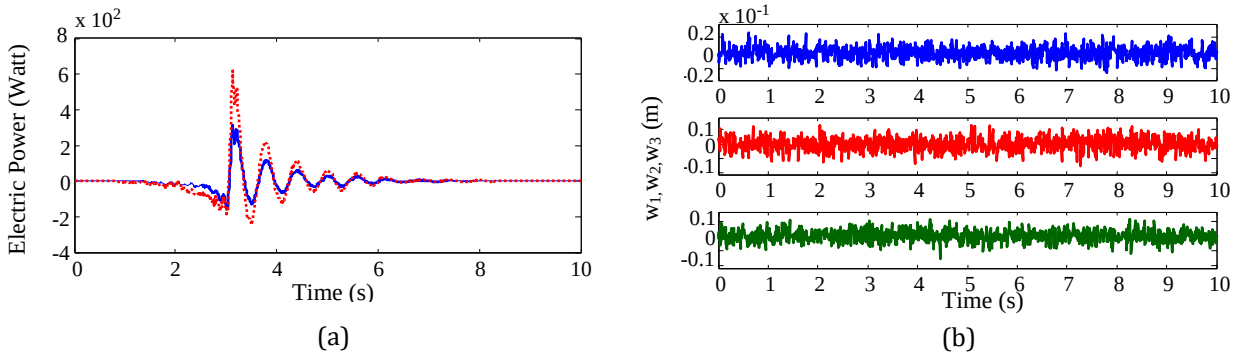

Figure 8 Harvested energy (a) Generated electric power (b) White noise time series

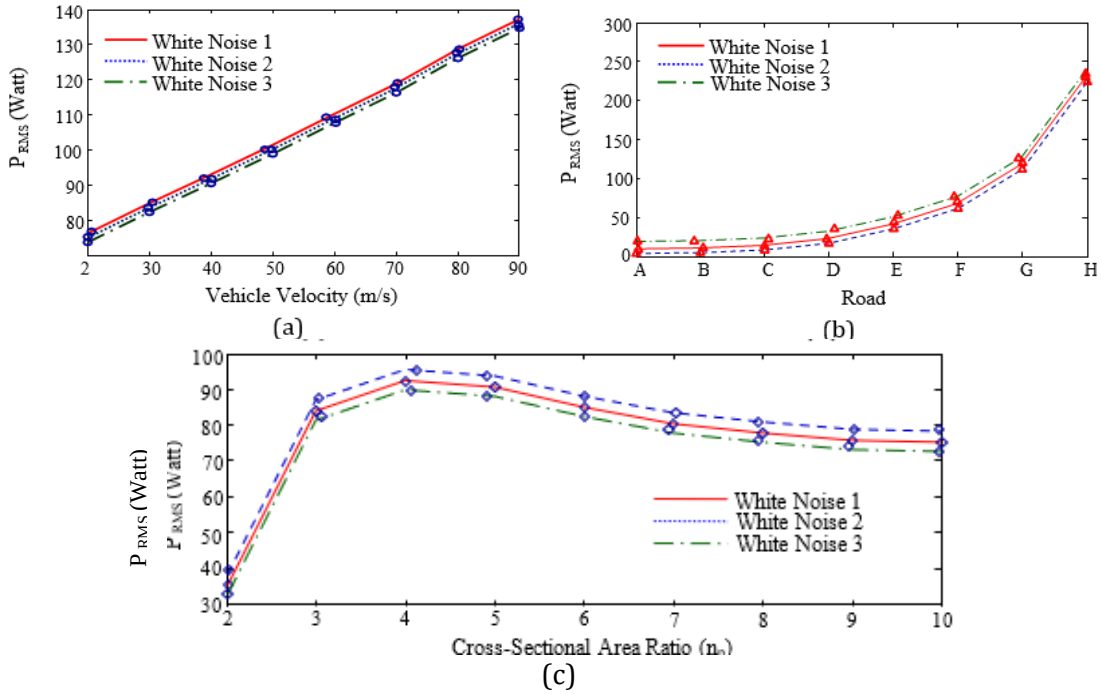

Figure 9 RMS of generated electric power under variation of (a) vehicle velocity (b) road class (c) piston cross-sectional area ratio

4. Conclusions

In this paper, a novel design of a PEH for a vehicle suspension system has been developed. The structural dynamics of the bridge, vehicle in terms of half-car model, and PEH system are characterized to calculate the RMS of generated electric power. The finding results show that the RMS of generated electric power increases with an increase in the velocity of vehicles, the ratio of the cross-sectional area of the piston cylinder, and the road roughness coefficient. The increment has a linear form for vehicle velocity variation and a nonlinear form for the last two variations. The electric power can be harvested up to 67.5 W for a PEH with a span of 150 m of the bridge, a velocity of 40 m/s, and a vehicle mass of 2,691.6 kg. Based on the findings, it is possible to harvest a higher power by increasing the number of PEHs, high-capacity type piezoelectric transducer, the size of the vehicle and speed, the number of passengers, and other parametric designs as long as the vehicle and PEH are safe. However, experimental work is envisaged for future work.

Acknowledgments

Financial support from Electronics and Information Research Organization under contract: SK IPT no. 2/III/HK/2022 and facility from Research Centre for Smart Mechatronics, National Research and Innovation Agency (BRIN) are greatly appreciated.

References

Akbar, M., Ramadhani, M.J., Izzuddin, M.A., Gunawan, L., Sasongko, R.A., Kusni, M., Curiel-Sosa, J.L., 2022. Evaluation on Piezoaeroelastic Energy Harvesting Potential of A Jet Transport Aircraft Wing with Multiphase Composite by means of Iterative Finite Element Method. *International Journal of Technology,* Volume 13(4), pp. 803–815

Alhumaid, S., Hess, D., Guldiken, R., 2022. A Noncontact Magneto–Piezo Harvester-Based Vehicle Regenerative Suspension System: An Experimental Study. *Energies*, Volume 15, p. 4476

Ali, A., 2015. Comparison Between Pakistani Corolla and Civic's Suspension: What's The Difference? Available Online at: https://www.pakwheels.com/blog/comparison-between-pakistani-corolla-and-civics-suspension-whats-the-difference/#:~:text=Both%20Civic%20and%20Corolla%20use,wishbone%20aka%20double%20A%20suspension, Accessed on June 14, 2021

Al-Yafeai, D., Darabseh, T., Mourad, A.-H.I., 2020. Energy Harvesting from Car Suspension System Subjected to Random Excitation. *In*: 2020 Advances in Science and Engineering Technology International Conferences (ASET). Presented at the 2020 Advances in Science and Engineering Technology International Conferences (ASET), IEEE, Dubai, United Arab Emirates, pp. 1–5

Aouali, K., Kacem, N., Bouhaddi, N., Haddar, M., 2021. On the Optimization of a Multimodal Electromagnetic Vibration Energy Harvester Using Mode Localization and Nonlinear Dynamics. *Actuators*, Volume 10, p. 25

Azangbebil, H., Djokoto, S.S., Chaab, A.A., Dragasius, E., 2019. A Study of Nonlinear Piezoelectric Energy Harvester with Variable Damping Using Thin Film MR Fluid. *IFAC Papers OnLine*, Volume 52-10, pp. 394–399

Chen, Y., Zhang, H., Zhang, Y., Li, C., Yang, Q., Zheng, H., Lü, C., 2016. Mechanical Energy Harvesting from Road Pavements Under Vehicular Load Using Embedded Piezoelectric Elements. *Journal of Applied Mechanics*, Volume 83, p. 081001

Darabseh, T., Al-Yafeai, D., Mourad, A.I., Almaskari, F., 2021. Piezoelectric Method-Based Harvested Energy Evaluation from Car Suspension System: Simulation and Experimental Study. *Energy Science & Engineering*, Volume 9, pp. 417–433

Du, R., Xiao, J., Chang, S., Zhao, L., Wei, K., Zhang, W., Zou, H., 2023. Mechanical Energy Harvesting in Traffic Environment and its Application in Smart Transportation. *Journal of Physics D: Applied Physics,* Volume 56, p. 373002

Elgamal, M.A., Elgamal, H., Kouritem, S.A., 2024. Optimized Multi-Frequency Nonlinear Broadband Piezoelectric Energy Harvester Designs. *Scientific Reports,* Volume 14, p. 11401

Ghormare, P., 2022. Development of Energy Harvesting Device to Utilize the Vibrational Energy of the Vehicle Suspension Systems. *In*: The 2nd International Conference on Innovative Research in Renewable Energy Technologies (IRRET 2022), *MDPI*, p. 10

Hendrowati, W., Guntur, H.L., Sutantra, I.N., 2012. Design, Modeling and Analysis of Implementing a Multilayer Piezoelectric Vibration Energy Harvesting Mechanism in the Vehicle Suspension. *Engineering,* Volume 4, pp. 728–738

Jeon, Y.B., Sood, R., Jeong, J.-h., Kim, S.-G., 2005. MEMS Power Generator with Transverse Mode Thin Film PZT. *Sensors and Actuators A: Physical*, Volume 122, pp. 16–22

Kulkarni, H., Zohaib, K., Khusru, A., Shravan Aiyappa, K., 2018. Application of Piezoelectric Technology In Automotive Systems. *Materials Today: Proceedings*, Volume 5, pp. 21299–21304

Lafarge, B., Delebarre, C., Grondel, S., Curea, O., Hacala, A., 2015. Analysis and Optimization of a Piezoelectric Harvester on a Car Damper. *Physics Procedia*, Volume 70, pp. 970–973

Lafarge, B., Grondel, S., Delebarre, C., Cattan, E., 2018. A Validated Simulation of Energy Harvesting with Piezoelectric Cantilever Beams on a Vehicle Suspension Using Bond Graph Approach. *Mechatronics*, Volume 53, pp. 202–214

Li, Z., Peng, Y., Xu, A., Peng, J., Xin, L., Wang, M., Luo, J., Xie, S., Pu, H., 2021. Harnessing Energy Form Suspension Systems of Oceanic Vehicles with High-Performance Piezoelectric Generators. *Energy*, Volume 228, pp. 1–14

Morangueira, Y.L.A., Pereira, J.C.C., 2020. Energy Harvesting Assessment with A Coupled Full Car and Piezoelectric Model. *Applied Energy*, Volume 210, pp. 1–13

Pan, P., Zhang, D., Nie, X., Chen, H., 2017. Development of Piezoelectric Energy-Harvesting Tuned Mass Damper. *Science China Technological Sciences,* Volume 60, pp. 467–478

Pasharavesh, A., Moheimani, R., Dalir, H., 2020. Nonlinear Energy Harvesting from Vibratory Disc-Shaped Piezoelectric Laminates. *Theoretical and Applied Mechanics Letters*, Volume 10, pp. 253–261

Piezo, n.d. Specification of Large Piezo Stack. Available Online at: http://www.piezo.com/prodstacks1.html, Accessed on April 10, 2020

Sheng, W., Xiang, H., Zhang, Z., Yuan, X., 2022. High-Efficiency Piezoelectric Energy Harvester for Vehicle-Induced Bridge Vibrations: Theory and Experiment. *Composite Structures*, Volume 299, p. 116040

Shin, Y.-H., Jung, I., Noh, M.-S., Kim, J. H., Choi, J.-Y., Kim, S., Kang, C.-Y., 2018. Piezoelectric Polymer-Based Roadway Energy Harvesting via Displacement Amplification Module. *Applied Energy*, Volume 216, pp. 741–750

Taghavifar, H., Rakheja, S., 2019. Parametric Analysis of the Potential of Energy Harvesting from Commercial Vehicle Suspension System. *In:* Proceedings of the Institution of Mechanical Engineers, Part D: Journal of Automobile Engineering, Volume 233(11), pp. 2687–2700

Tao, J.X., Viet, N.V., Carpinteri, A., Wang, Q., 2017. Energy Harvesting from Wind by a Piezoelectric Harvester. *Engineering Structures*, Volume 133, pp. 74–80

Tavares, R., Ruderman, M., 2020. Energy Harvesting Using Piezoelectric Transducers for Suspension Systems. *Mechatronics*, Volume 65, pp. 1–9

Tian, L., Shen, H., Yang, Q., Song, R., Bian, Y., 2023. A Novel Outer-Inner Magnetic Two Degree-Of-Freedom Piezoelectric Energy Harvester. *Energy Conversion and Management*, Volume 283, p. 116920

Touairi, S., Mabrouki, M., 2021. Control and Modelling Evaluation of a Piezoelectric Harvester System. *International Journal of Dynamics and Control*, Volume 9, pp. 1559–1575

Viet, N.V., Al-Qutayri, M., Liew, K.M., Wang, Q., 2017. An Octo-Generator for Energy Harvesting Based on The Piezoelectric Effect. *Applied Ocean Research*, Volume 64, pp. 128–134

Wang, M., Yin, P., Li, Z., Sun, Y., Ding, J., Luo, J., Xie, S., Peng, Y., Pu, H., 2020. Harnessing Energy from Spring Suspension Systems with A Compressive-Mode High-Power-Density Piezoelectric Transducer. *Energy Conversion and Management*, Volume 220, pp. 1–12

Wei, C., Taghavifar, H., 2017. A Novel Approach to Energy Harvesting from Vehicle Suspension System: Half-Vehicle Model. *Energy*, Volume 134, pp. 279–288

Wu, N., Wang, Q., Xie, X., 2015. Ocean Wave Energy Harvesting with A Piezoelectric Coupled Buoy Structure. *Applied Ocean Research*, Volume 50, pp. 110–118

Xie, L., Cai, S., Huang, G., Huang, L., Li, J., Li, X., 2020. On Energy Harvesting from a Vehicle Damper. *IEEE/ASME Transactions on Mechatronics*, Volume 25(1), pp. 108–117

Xie, X.D., Wang, Q., 2015. Energy Harvesting from a Vehicle Suspension System. *Energy*, Volume 86, pp. 385–392

Zhao, Z., Wang, T., Shi, J., Zhang, B., Zhang, R., Li, M., Wen, Y., 2019a. Analysis and Application of The Piezoelectric Energy Harvester on Light Electric Logistics Vehicle Suspension Systems. *Energy Science & Engineering*, Volume 7(6), pp. 2741–2755

Zhao, Z., Wang, T., Zhang, B., Shi, J., 2019b. Energy Harvesting from Vehicle Suspension System by Piezoelectric Harvester. *Mathematical Problems in Engineering*, pp. 1–10